Supplementary Material - Quantum storage of three-dimensional orbital-angular-momentum entanglement in a crystal

Zong-Quan Zhou,[1,2] Yi-Lin Hua,[1,2] Xiao Liu,[1,2] Geng Chen,[1,2] Jin-Shi Xu,[1,2] Yong-Jian Han,[1,2] Chuan-Feng Li*,[1,2] and Guang-Can Guo[1,2]

[1]*Key Laboratory of Quantum Information, University of Science and Technology of China, CAS, Hefei, 230026, China*
[2]*Synergetic Innovation Center of Quantum Information and Quantum Physics, University of Science and Technology of China, Hefei, 230026, P.R. China*

(Dated: July 18, 2015)

I. DETAILS OF THE SETUP

The master laser is a Ti:Sapphire laser (MBR-110, coherent) with a frequency of 340.6966 THz. The frequency of the master laser is stabilized to a low-drift Fabry-Pérot Interferometer (FPI). The FPI is constructed from ultra-low-expansion glass. It is placed in a high-vacuum housing and its temperature is stabilized. The linewidth of the master laser is less than 50 kHz, and there is no observable frequency drift during the experiments.

Part of the laser output is fed into a cavity-enhanced frequency doubler to generate blue light. The blue light is controlled with a -200-MHz acousto-optic modulator (AOM1) in the single-pass configuration. The power of the 440-nm pump light is maintained at 50 mW for the measurements unless otherwise noted. The photon pairs are filtered by etalon1 (free spectral range of 105 GHz, and linewidth of 1.4 GHz) and the etalon2 (free spectral range of 50 GHz, and linewidth of 700 MHz). The two etalons are calibrated using a reference laser beam at a frequency of $\nu_0 = 340.6965$ THz. The temperature drift of the etalons is less than 10 mK. The resonant laser transmission efficiency is greater than 95% for both etalons. After passing through the two etalons, the two photons have exactly the same frequency and a bandwidth of approximately 700 MHz. This claim is supported by the low transmission efficiency ($< 1\%$) of the photons through our memory sample (see Fig. S6(a)).

The detailed lens configuration of the setup is illustrated in Fig. S1. The photon source is imaged to the first polarization beam splitter (PBS) through a lens with $f = 100$ mm and another lens with $f = 300$ mm. After the PBS, the idler photon is forced to propagate through a 16.4-m-long delay line. The delay line consists of six $4f$ systems, two of which are formed with $f = 300$ mm, two with $f = 750$ mm and the remaining two with $f = 1000$ mm, resulting in a total propagation distance of 16.4 m. The quarter-wave plate (QWP) located before the final reflection mirror is set at 22.5 degrees, thus rotating the polarization of the photons back to vertical. The photons are therefore reflected when they are again incident on the PBS and are analyzed using the spatial light modulators (SLM1, BNS, 512×512) and the single-mode fiber (SMF). The transmission efficiency of the double-pass delay line is approximately 68%. The double-pass delay line ensures that during the storage process of the signal photon, the idler photon is propagating in free space rather than being detected.

The signal photons are directed to the quantum memory through two $4f$ systems consisting two pairs of lenses with focal lengths of $f = 300$ mm and $f = 750$ mm. Another portion of the master laser output is used for preparation of atomic frequency comb (AFC). AOM2 with a center frequency of -250 MHz, is used in the double-pass configuration to down-shift the laser frequency. AOM3 has a center frequency of 200 MHz and is also used in the double-pass configuration. Thus, the center frequency for the AFC preparation matches that of the photon source: $\nu_0 = 340.6965$ THz.

The AFC preparation light and the signal photons are combined by the $f = 300$ mm lens and overlap at the sample position. The Gaussian mode of the signal photons is focused to a diameter of approximately 130 μm. The beam diameter of the pump light is approximately 2 mm at the sample position. The sample is placed in a cryostat at a temperature of 1.5 K and under a superconducting magnetic field of 0.3 T in the horizontal direction. The c-aixs of the Nd^{3+}:YVO_4 crystal is oriented in the horizontal direction. The crystal strongly absorbs only horizontally-polarized light; when the polarization of the incident photons is rotated to horizontal, then the photons are absorbed and stored in the crystal. The quantum states of the input photons are analyzed by rotating the polarization of the input photons to vertical to ensure little absorption.

Photons carrying orbital-angular momentum (OAM) can be well described in cylindrical coordinates using Languerre-Gauss modes (LG_{pl}). The index l is referred to as the azimuthal number, and p is the radial number. Here, we only consider the case of $p = 0$. We encode qudits using the LG modes of the photons, with eigenstates defined in terms of the azimuthal index l. LG beams with an index of l carry an OAM of $l\hbar$ per photon [1], and the Gaussian mode can be regarded as $LG_{0,0}$. The OAM states of the transmitted or stored signal photons are analyzed using SLM2 (BNS, 512×512) and the SMF. The

*email:cfli@ustc.edu.cn

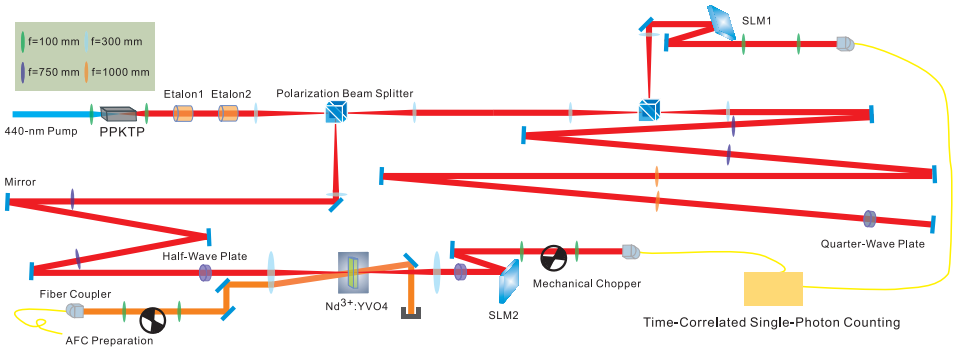

Fig. S1: Detailed lens configuration. The idler photon is forced to propagate through a double-pass delay line which consists of six $4f$ systems. The signal photon is directed to the quantum memory through two 4f systems. The orbital-angular momentum states of the photon pairs are analyzed with spatial light modulators (SLM) and single-mode fiber.

two SLMs used in the experiment have diffraction efficiencies of 94% and 96% for a laser at 880 nm. The SLMs, which have different phase patters, convert different modes into Gaussian modes, and the SMF projects the incoming photons into the fundamental mode of the fiber which is a nearly Gaussian mode with $l = 0$ and $p = 0$. The typical extinction ratio for the $\mathrm{LG}_{0,-1}$, $\mathrm{LG}_{0,0}$ and $\mathrm{LG}_{0,1}$ modes is greater than 300:1. The extinction ratio for higher dimensions is typically greater than $100:1$ for various l values.

The preparation and measurement timing is controlled by arbitrary function generators (AFG, Tektronix, AFG3252). The AFC preparation requires 12.5 ms after which the pump light is completely blocked the chopper located in the path of the pump beam. To avoid fluorescence noise caused by the classical pump light, the measurement phase begins 1.5 ms after the preparation is complete. The measurement cycle lasts for a time of 10 ms, during which the signal photons are stored in the crystal. Complete cycles of preparation and measurement are repeated at a frequency of 40 Hz. The chopper located before single-photon detector (SPD) is opened during the measurement phase to enable the detection of single photons.

II. CONCENTRATION OF ENTANGLEMENT

Most of the current applications of entanglement in quantum information processing function best for the maximally-entangled state (MES). However, in practice, most sources can only generate non-maximally entangled states. Therefore, concentration has been used to enhance the quality of entanglement. The experimental concentration of OAM entanglement has been achieved by moving the lens [2] and by altering the diffraction efficiencies and different modes [3] for sources based on spontaneous parametric down-conversion (SPDC) in short BBO crystals. The OAM-entangled photons are typically generated with thin BBO crystal to increase the mode capacity. However, the generated photons have a typical bandwidth of several nm which is not suitable for interface with other systems.

Here we used a 20-mm PPKTP crystal to generate OAM-entangled photons with initial bandwidth of approximately 200GHz. The quality of entanglement is low for the photon pairs that are directly generated from the 20-mm-long PPKTP crystal. A three-step concentration procedure is applied to enhance the qutrit-qutrit entanglement. A pair of lenses with $f = 100$ mm is placed before the fiber coupler for each photon. The spacing between these two lenses is carefully adjusted to achieve the first step of entanglement concentration. As shown in Fig. S2, if the $\mathrm{LG}_{0,0}$ modes are collected with the the maximum possible efficiency, the the ratios of generation probabilities of the Gaussian modes and the LG modes are greater than 11:1, which indicates that little entanglement can be achieved. A more balanced relative amplitude can be achieved by decreasing the lens spacing by 3.25 mm for both sides. After the lens are adjusted in this manner, the photon pair entanglement has a fidelity of 0.542 ± 0.002 with respect to the MES $|\psi_0\rangle = (|-1\rangle|1\rangle - |0\rangle|0\rangle + |1\rangle|-1\rangle)/\sqrt{3}$. The reconstructed density matrix is illustrated in Fig. S3. Here, the measurement basis are given in Fig. S11, which follows the definition in previous work [4]. The phase item between $|-1\rangle|1\rangle$ and $|0\rangle|0\rangle$ is determined by definition of the chosen measurement basis. As discussed in [2], it is always possible to choose the basis for describing the state in Eq.1 in the main text so that there are no relative phases between the components.

Then, the two etalons are inserted in the beam path. The photon pairs must be resonant with both the two etalons simultaneously to achieve coincidence. As shown in Fig. S3, the optimal phase-matching temperature is slightly different for photons with $l = \pm 1$ compared with that for Gaussian modes. This difference occurs because the divergence of an orbital-angular-momentum-carrying beam [5] (further discussions of the photon source will be presented elsewhere). Note that the application of two

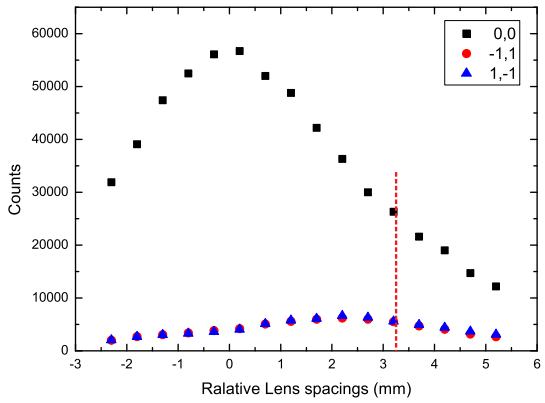

Fig. S2: Tuning the collection efficiency for the Gaussian mode and the $LG_{0,\pm1}$ modes by modifying the lens spacing.

etalons not only decreases the bandwidth of the photon source but also allows significant enhancement of the entanglement to be achieved. One possible reason for this enhancement is the effective increase in the photon coherence time that results from the time-energy uncertainty relation.

According to Fig. S4, great care must be taken in tuning the temperature of the PPKTP crystal. If the temperature is set to 44 degrees which is the optimal phase matching temperature for Gaussian modes. Then the strongly imbalance in the probabilities of generating Gaussian modes and LG modes will again destroy the entanglement. With the two etalons inserted in the beam path and the temperature of the PPKTP crystal set to 42 degrees which is approximately the optimal phase-matching temperature for $LG_{0,\pm1}$ modes, the fidelity with respect to the MES significantly increased to 0.666 ± 0.005. Fig. S5 presents the reconstructed density matrix for such states.

The final step of the entanglement concentration is achieved by further tuning the temperature of the PPKTP crystal to 41.25 degrees. This operation further balances the relative amplitudes between the Gaussian modes and the $LG_{0,\pm1}$ modes, although at the expense of a small degradation in photon counts. The final states have a fidelity to the MES of 0.730 ± 0.006 and are presented in Fig. 2a in the main text.

This fidelity is still away from unity. Two reasons can be considered. The major diagonal elements of the reconstructed density matrix are $\langle -1,1|\rho|-1,1\rangle$=0.206,$\langle 0,0|\rho|0,0\rangle$=0.466, $\langle 1,-1|\rho|1,-1\rangle$=0.216. The summation of remaining elements is 1-(0.206+0.466+0.216)=0.112, represents the components of nonzero total OAM for the photon pair. From the three-step concentration of entanglement, one can notice that the imbalance of the diagonal elements also strongly affects the fidelity. Further improvements can also be achieved by introducing blazed phase gratings into the SLMs and altering the diffraction efficiencies for different modes [3]. For generation at higher-dimensional entanglement, the pump light should be collimated to give larger beam waist at the nonlinear crystal.

For the measurement of the input states, the typical coincidence rate is 140 per second. Considering the photon loss during the propagation in the delay line and in the cryostat, we estimate that the production rate of the photon source is approximately 500 paris per second, which is two orders of magnitude brighter than that can be achieved via spontaneous Raman scattering in an atomic ensemble [4]. The typical measurement times for the quantum state tomography of the input states and the retrieved states are approximately 50 minutes and 5 hours, respectively.

Photons are the messenger in quantum networks. High dimensional encoding can significantly improve the data rate. Such flexible photon source can find important applications in the quantum interface among various physical systems in networks, for example, the quantum dot, NV and trapped ions. These systems have their particular working wavelength and bandwidth that should be matched with the user-defined photon source.

III. AFC STORAGE OF PHOTONIC ENTANGLEMENT

The AFC protocol requires a tailored absorption profile with a series of narrow, periodic absorption peaks separated by Δ. The single-photon input is then collectively absorbed and diffracted by the atomic frequency grating. An atomic state with single-photon excitation can be represented by [6] $|e\rangle_N = \sum_j^N c_j e^{-ikz_j} e^{i2\pi\delta_j t} |g_1 \cdots e_j \cdots g_N\rangle$, where N is the total number of atoms in the comb; $|g_j\rangle$ and $|e_j\rangle$ represent the ground and excited states, respectively, of atom j; z_j is the position of atom j; k is the wavenumber of the input field; δ_j is the detuning of the atom with respect to the laser frequency and the amplitudes c_j depend on the frequency and on the position of atom j. Because of the periodical structure of the AFC, $\delta_j \simeq m_j\Delta$, where m_j is an integer. In the experiment, AOM3 is controlled by a computer-generated 'image' that determines both the intensity and the frequency of the diffracted beam. In this way, a high-contrast comb with a Δ of 25 MHz and a bandwidth of 100 MHz is constructed. The storage efficiency for weak coherent pulses with a temporal width of 20 ns is approximately 31%.

To further enlarge the bandwidth of the AFC, a free-space phase -electro-optic modulator(EOM) with a resonance frequency of 300 MHz and a fiber-coupled phase -EOM with a modulation frequency of 100 MHz are used to generate frequency sidebands [7]. The driving voltages V_{p-p} are carefully adjusted to achieve optimal modulation for both EOMs, with modulation index β close to 1.4 rad. The resulting first-order and second-order sidebands

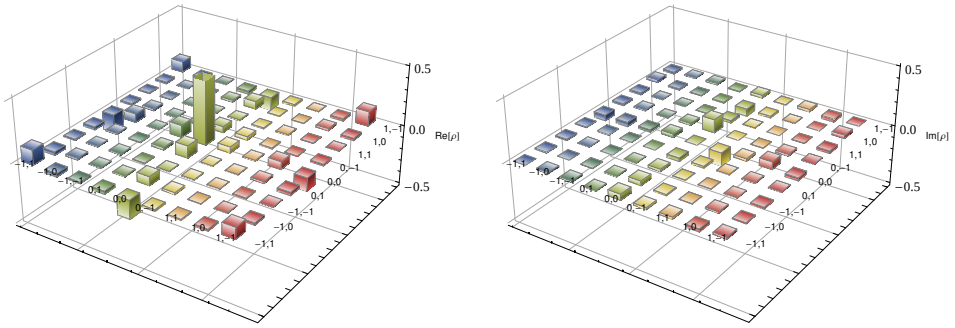

Fig. S3: Density matrix of the entanglement without the etalons. The power of the blue pump light is 1 mW, and the integration time is 3 s.

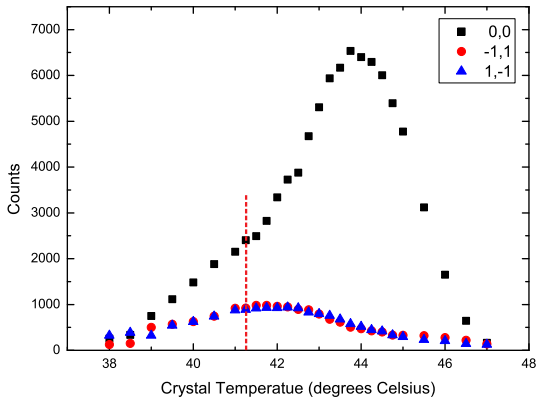

Fig. S4: Tuning the production rate of degenerate photon pairs in different modes by changing the crystal temperature.

exhibit frequency shifts of ±100 MHz, ±200 MHz, ±300 MHz and ±600 MHz. The frequency mixing that occurs in the two EOMs will also generate sidebands with frequency shifts of ±200 MHz, ±400 MHz and ±500 MHz, etc. In this manner, the comb at the center frequency is copied to all sidebands, and an overall AFC bandwidth of approximately 1 GHz is expected.

An example of the storage and retrieval process for photons that generated by the narrow-band SPDC source is presented in Fig. S6. The idler photon is detected with an OAM state of $|-1\rangle+|1\rangle$, which collapses the signal-photon states to $|-1\rangle+|1\rangle$. The input states are shown as the black line, and the readout states with $|-1\rangle+|1\rangle$ are shown as the red line. With a coincidence window of 2 ns, a storage efficiency of approximately 20% can be calculated from these results. The small degradation in efficiency compared with that achieved for the weak coherent pulses can be attributed to the lower quality of the AFC carried by the sidebands. Nevertheless, the storage efficiency achieved here is several times greater than that achieved with Nd^{3+} doped YSO crystals [7]. The readout photons with OAM states specified by $|-1\rangle-|1\rangle$ are also present as the blue lines in the figure. Vanishing photon counts can be observed for such states demonstrating the high purity of the entanglement and the reliability of the quantum memory. From the temporal spectrum of the two photons, the normalized cross-intensity correlation after storage can be calculated $g^{(2)}_{i,s}=P_{si}/P_sP_i$. P_{si} (P_sP_i) can be estimated from the number of coincident counts in a detection window centered one (far from) the coincidence peak. Using a detection window of 2 ns, a value of $g^{(2)}_{i,s}\simeq 330$ is obtained for the retrieved photons.

Note that the power of the AFC preparation light here is selected for optimized and balanced AFC efficiency for Gaussian modes and $LG_{0,\pm1}$ modes. The power consumption is approximately 3 mW (0.6 mW) with (without) the EOMs in operation.

IV. VIOLATION OF A 3-DIMENSIONAL BELL-TYPE INEQUALITY

The Bell expression in three dimensions is [8]

$$\begin{aligned} S \equiv & [P(A_1=B_1)+P(B_1=A_2+1) \\ & +P(A_2=B_2)+P(B_2=A_1)] \\ & -[P(A_1=B_1-1)+P(B_1=A_2) \\ & +P(A_2=B_2-1)+P(B_2=A_1-1)], \end{aligned} \tag{1}$$

where

$$P(A_a=B_b+k)\equiv\sum_{j=0}^{2}P(A_a=j,B_b=j+k mod 3) \tag{2}$$

denotes the probabilities of joint measurements on the signal and idler photons. A_1, A_2 and B_1, B_2 denote two possible settings of the local analyzers on each side. Each measurement has three possible outcomes, denoted by 0, 1, or 2. For theories based on local realism, S satisfies the inequality $S\leq 2$. By contrast, quantum mechanics suggests that 3-d entanglement should lead to the violation of this inequality.

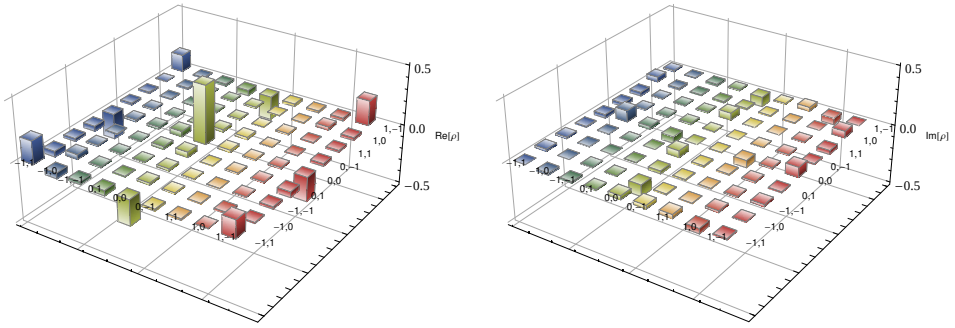

Fig. S5: Entanglement of the photon pairs after spectral filtering by the two etalons. The temperature of the PPKTP crystal is set to 42 degrees.

	$P(A_1 = B_1)$	$P(B_1 = A_2 + 1)$	$P(A_2 = B_2)$	$P(B_2 = A_1)$	$P(A_1 = B_1 - 1)$	$P(B_1 = A_2)$	$P(A_2 = B_2 - 1)$	$P(B_2 = A_1 - 1)$
E_{in}	0.716 ± 0.014	0.654 ± 0.013	0.615 ± 0.013	0.861 ± 0.016	0.170 ± 0.006	0.196 ± 0.006	0.258 ± 0.007	0.071 ± 0.003
E_{out}	0.712 ± 0.015	0.704 ± 0.015	0.565 ± 0.013	0.889 ± 0.017	0.195 ± 0.007	0.153 ± 0.006	0.320 ± 0.009	0.050 ± 0.003

Table S1:Measured correlation coefficients required to test the 3-d Bell inequality. Uncertainties represent one standard deviation based on Poissonian detection statistics. The measurements for S without memory are are performed for a duration of 15 min; those with memory are performed for a duration of 2.5 hours.

In accordance with the definition of S, we use the general steepest descent method to chooses the measurement basis for the violation of the Bell inequality in 3 dimensions. The reconstructed density matrix obtained through quantum state tomography is used as the input state. The steepest descent method may become trapped at a local minimum (or maximum); it is not guaranteed that the result will provide the global optimization. The locally optimized basis corresponds to the following states. For the idler photon, $A_{11} = (-0.044, -0.998, -0.044)$, $A_{12} = (-0.994, 0.039, 0.105)$, $A_{13} = (0.103, -0.048, 0.993)$, $A_{21} = (-0.316, 0.691, 0.650)$, $A_{22} = (-0.655, -0.655, 0.377)$, and $A_{23} = (-0.687, 0.306, -0.659)$. For the signal photon, $B_{11} = (-0.332, -0.894, 0.300)$, $B_{12} = (-0.352, -0.178, -0.919)$, $B_{13} = (-0.875, 0.410, 0.256)$, $B_{21} = (-0.139, 0.961, 0.239)$, $B_{22} = (0.338, 0.273, -0.901)$, and $B_{23} = (0.931, 0.045, 0.362)$. The ket space is $\begin{pmatrix} |-1\rangle \\ |0\rangle \\ |1\rangle \end{pmatrix}$. The expected values of S are 2.164 and 2.189 for the entanglement before and after storage, respectively. The measurement basis is not optimized; however, the experimentally measured value $S = 2.152 \pm 0.033$ is sufficiently strong to violate the predictions of local realistic models. The resulting correlation coefficients are presented in Table S1. The patterns of the SLMs for achieving these measurements are depicted in Fig. S7.

V. QUANTUM PROCESS TOMOGRAPHY

For the measurements presented in Fig. 3 in the main text, another 200-MHz -AOM in the double-pass configuration is used to generate weak coherent pulses with a frequency of ν_0 and a temporal width of 20 ns. The pulses are attenuated to approximately 0.5 photons per pulse using neutral density filters. For this measurement, 10000 trials of single-photon pulses with a periodicity of 200 ns are stored in the sample during the measurement phase. The mean number of input photons is determined by measuring the detection probability per pulse with the polarization of the input photons rotated to V, while accounting for the detection efficiency (~ 0.4) and the transmission from the sample to the detector (~ 0.6). For the measurements presented in Fig. 3, the power of the pump light is the same as that used for the storage of three-diomensional entanglement. The probe field is carefully collimated to achieve a beam diameter of approximately 2 mm at SLM1 and focused to a diameter of approximately 130 μm at the sample position. SLM1, the memory hardware, SLM2 and the two lenses with $f = 300$ mm collectively constitute a $4f$ imaging system. SLM1 is the mask plane, the memory is the Fourier plane, and SLM2 represents the image plane.

The photonic qutrits are generated at SLM1 as shown in Fig. 3a. The final states are analyzed using the SLM2 and the SMF. This process (with or without the memory) can be regarded as a state-transfer process and can be represented by a quantum process χ [10]. The output

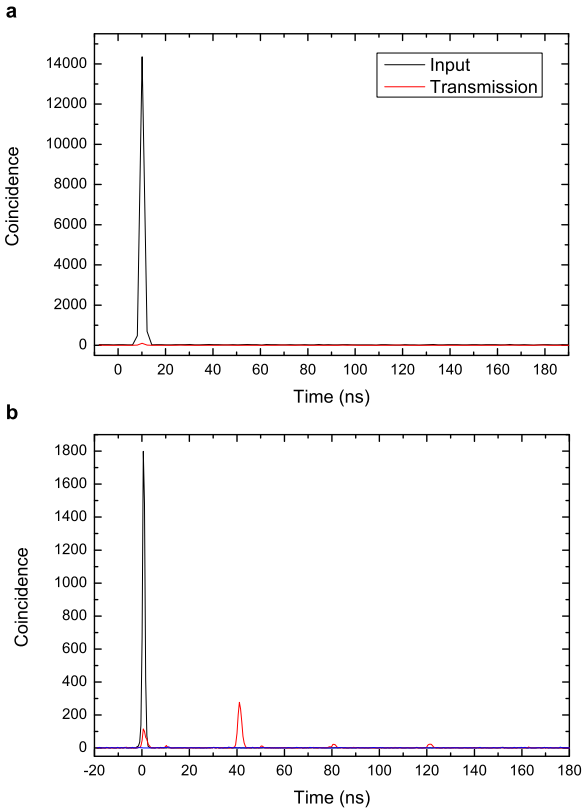

Fig. S6: (a). Coincidence histograms in 1 second for the photon source in Gaussian mode before and after the sample absorption. A pump power of approximately 200 mW is used to achieve high brightness. The cross-correlation is still very good ($g^{(2)}_{i,s} > 400:1$), however the PPKTP crystal can be easily damaged by the high-power pump laser. The bandwidth of the photon source is approximately 700 MHz. More than 99% of the input photons is absorbed by the sample. (b). Coincidence histograms for the AFC storage of photonic entanglement. The pump power is maintained at 50 mW. The black line represents the input states with OAM states projected to $|-1\rangle + |1\rangle$. The red line represents the coincidence histogram for a programmed storage time of 40 ns. The blue represents the coincidence for a measurement basis of $|-1\rangle - |1\rangle$; as expected, vanishing coincidence is observed.

state can be represented by

$$\rho_{out} = \sum_{m,n=1}^{9} \chi_{mn} \lambda_m \rho_{in} \lambda_n^{\dagger}, \tag{3}$$

where λ_m is the basis for operators acting on the input state ρ_{in} and $\dagger$ denotes the adjoint operator. The matrix χ completely and uniquely describes the process and can be reconstructed by measuring the output state s ρ_{out} for a number of different input states. The complete operators for the reconstruction of the matrix χ are as follows [11]: $\lambda_1 = \begin{pmatrix} 1 & 0 & 0 \\ 0 & 1 & 0 \\ 0 & 0 & 1 \end{pmatrix}$, $\lambda_2 = \begin{pmatrix} 0 & 1 & 0 \\ 1 & 0 & 0 \\ 0 & 0 & 0 \end{pmatrix}$, $\lambda_3 = \begin{pmatrix} 0 & -i & 0 \\ i & 0 & 0 \\ 0 & 0 & 0 \end{pmatrix}$, $\lambda_4 = \begin{pmatrix} 1 & 0 & 0 \\ 0 & -1 & 0 \\ 0 & 0 & 0 \end{pmatrix}$, $\lambda_5 = \begin{pmatrix} 0 & 0 & 1 \\ 0 & 0 & 0 \\ 1 & 0 & 0 \end{pmatrix}$, $\lambda_6 = \begin{pmatrix} 0 & 0 & -i \\ 0 & 0 & 0 \\ i & 0 & 0 \end{pmatrix}$, $\lambda_7 = \begin{pmatrix} 0 & 0 & 0 \\ 0 & 0 & 1 \\ 0 & 1 & 0 \end{pmatrix}$, $\lambda_7 = \begin{pmatrix} 0 & 0 & 0 \\ 0 & 0 & -i \\ 0 & i & 0 \end{pmatrix}$, and $\lambda_9 = \frac{1}{\sqrt{3}} \begin{pmatrix} 1 & 0 & 0 \\ 0 & 1 & 0 \\ 0 & 0 & -2 \end{pmatrix}$. The input states $|\psi_i\rangle (i = 1, 2, ...9)$ are chosen to be $|-1\rangle, |0\rangle, |1\rangle, (|0\rangle + |-1\rangle)/\sqrt{2}, (|0\rangle + |1\rangle)/\sqrt{2}, (|0\rangle + i|-1\rangle)/\sqrt{2}, (|0\rangle - i|1\rangle)/\sqrt{2}, (|-1\rangle + |1\rangle)/\sqrt{2}, (|-1\rangle + i|1\rangle)/\sqrt{2}$, respectively. By preparing these nine input states and measuring the corresponding output states in 9 basis vectors represented by the operators $u_i \otimes u_j$ $(i, j = 1, 2, ...9, u_i = |\psi_i\rangle\langle\psi_i|)$, the process matrix χ can be reconstructed using the maximum-likelihood procedure based on the 81 measurements according to Eq. 1. The process matrix without the memory is denoted by χ_1 and for the ideal process, this matrix should be $\chi_0 = \begin{pmatrix} 1 & 0 & 0 & 0 & 0 & 0 & 0 & 0 & 0 \\ 0 & 0 & 0 & 0 & 0 & 0 & 0 & 0 & 0 \\ 0 & 0 & 0 & 0 & 0 & 0 & 0 & 0 & 0 \\ 0 & 0 & 0 & 0 & 0 & 0 & 0 & 0 & 0 \\ 0 & 0 & 0 & 0 & 0 & 0 & 0 & 0 & 0 \\ 0 & 0 & 0 & 0 & 0 & 0 & 0 & 0 & 0 \\ 0 & 0 & 0 & 0 & 0 & 0 & 0 & 0 & 0 \\ 0 & 0 & 0 & 0 & 0 & 0 & 0 & 0 & 0 \\ 0 & 0 & 0 & 0 & 0 & 0 & 0 & 0 & 0 \end{pmatrix}$. The fidelity of this quantum process can be calculated as $[Tr(\sqrt{\sqrt{\chi_1}\chi_0\sqrt{\chi_1}})]^2$. The process matrix with the memory, which is reconstructed through measurements of the retrieved photons, is denoted by χ_2. An ideal quantum memory should produce a process matrix that is exactly identical to χ_1. The fidelity of the memory process can be calculated as $[Tr(\sqrt{\sqrt{\chi_2}\chi_1\sqrt{\chi_2}})]^2$.

The operators $u_i \otimes u_j$ are applied by the two SLMs in combination with the SMF to achieve the quantum process tomography in 3 dimensions. The patterns applied on SLM1 and SLM2 to achieve the preparation and measurement of vectors $|\psi_i\rangle$ $(i = 1, 2, ...9)$ are depicted in Fig. S12. Notably, the measurement vectors at the image plane must be converted to the conjugates of the corresponding input states because of the conjugate properties between the mask plane and the image plane in a $4f$ system.

The reconstructed process matrix χ_1 of the setup without the memory is presented in Fig. S8a. The measurements on the transmitted photons are performed by rotating the polarization of the input photons to ver-

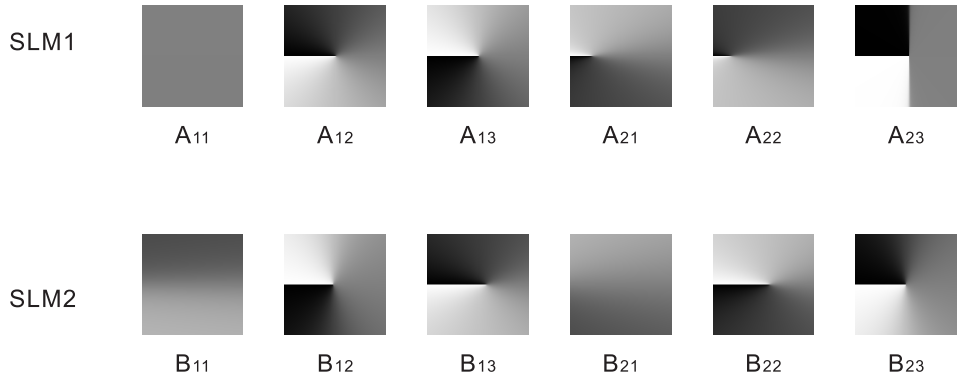

Fig. S7: SLM patterns for measurements of Bell inequality.

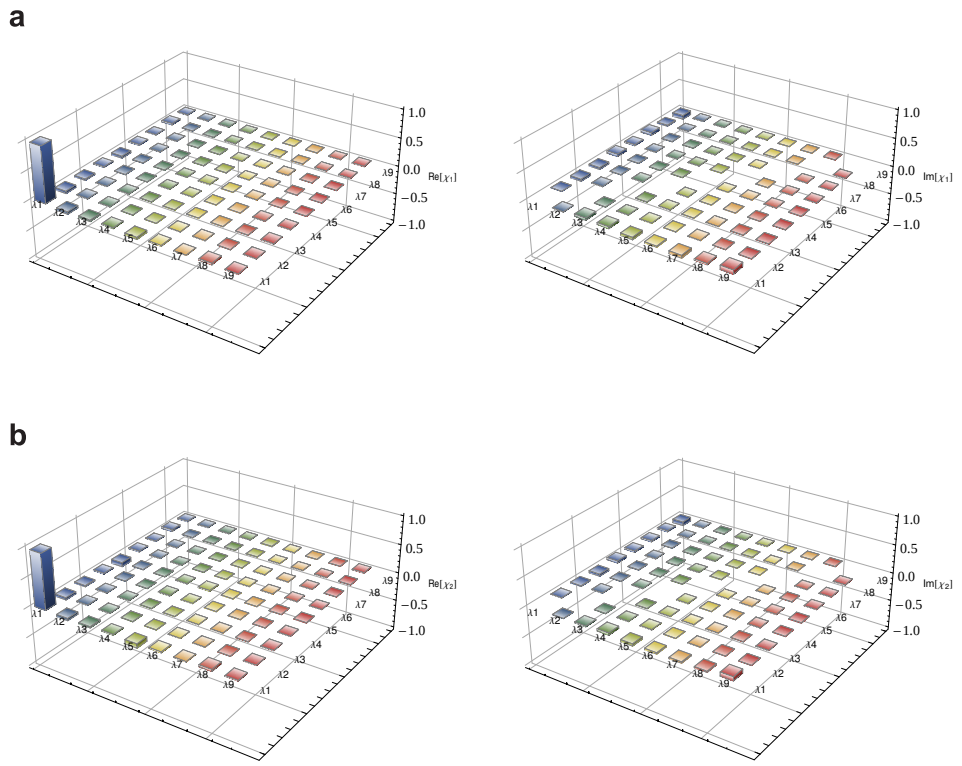

Fig. S8: Reconstructed quantum process of the setup without (a) and with (b) quantum memory as obtained through quantum process tomography.

tical to avoid sample absorption. The half-wave plate (HWP) after the cryostat must also be adjusted to ensure that SLM2 is in operation. The fidelity of χ_1 is 0.970 ± 0.001, slightly lower than 100%; there are several possible reasons for this slight deviation from the ideal case. First, note that the mode conversions between the $\mathrm{LG}_{0,\pm1}$ modes and the Gaussian modes are not perfect and that the SMF coupling efficiencies for mode-converted photons are significantly lower than the coupling efficiency for pure Gaussian modes. In our experiment, the coupling efficiency for Gaussian modes into an SMF is approximately 90% whereas the coupling efficiency for converted $\mathrm{LG}_{0,\pm1}$ modes is 80% $\sim$ 86%. Second, non-ideal position matching between the two SLMs and the beam center could further reduce the fidelity.

Although the setup exhibits non-ideal operation for LG modes, the memory process χ_2 reconstructed from measurements of the retrieved photons exhibits a high fidelity (0.993 ± 0.002) with respect to χ_1. These results demonstrate the reliability of the quantum memory for the 3 considered dimensions.

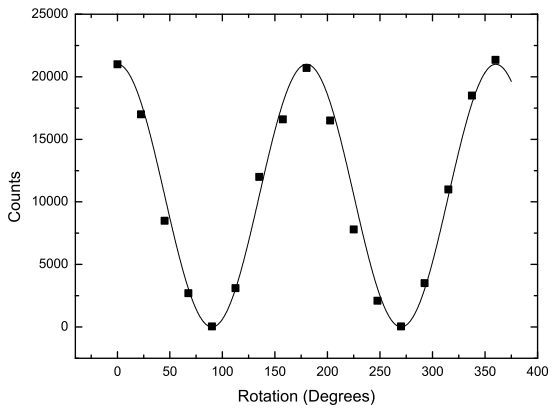

Fig. S9: Detailed measurements of the superposition state $|-1\rangle + |1\rangle$. The black dots represent the measured results, and the line represents a sinusoidal fit to the data.

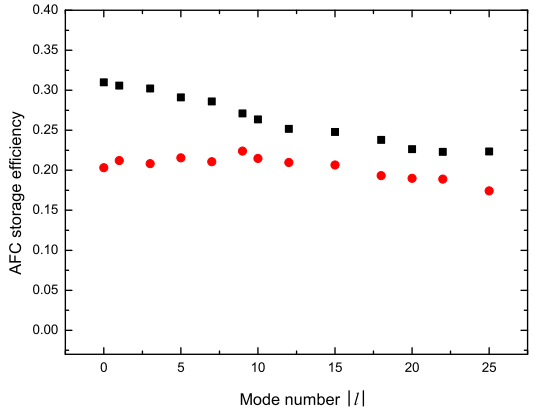

Fig. S10: The AFC storage efficiency for $|\psi_+(l)\rangle$ states. The black squares represent the results obtained by independently optimizing the pump power for different $|l|$, and the red dots represent a balanced AFC efficiency for all modes with a pump power of approximately 3 mW without EOM modulation.

VI. STORAGE PERFORMANCE FOR SUPERPOSITON STATES IN HIGH DIMENSIONAL SPACES

For higher dimensional spaces, quantum process tomography is no longer an efficient method for characterizing the memory process. The visibility of superposition states in higher dimensional spaces is used to benchmark the memory performance. As shown in Fig. 3c in the main text, our memory exhibits an excellent visibility performance for states spanning 51 dimensions, indicating that the coherence among different LG modes is well preserved during the storage process.

As an example, we present more detailed measurements of the superposition states of $|-1\rangle + |1\rangle$. The pattern on SLM1 is programmed to prepare the required superposition state $|-1\rangle+|1\rangle$ (the normalized coefficients are omitted for simplicity), whereas the measurement basis, as controlled by SLM2, is $|-1\rangle + e^{i*2\theta}|1\rangle$, with θ varying from 0 to 360 degrees. The patterns applied on the SLM to achieve these measurements are depicted in Fig. 12b. The measured results are presented in Fig. S9. The photon counts exhibit a sinusoidal oscillation, as expected.

A seemingly probabilistic decrease in storage efficiency is observed for higher $|l|$. This is not a fundamental problem; it is simply caused by the fact that the power of the pump light is optimized for storage efficiency for $l = 0$ and $l = \pm 1$. The different power consumption of the pump light for different $|l|$ is caused by the increase in the beam diameter for higher $|l|$ and the spatially non-flat intensity profile of the Gaussian pump light.

As indicated by the red dots in Fig. S8, balanced efficiency for all modes can be achieved with a pump power of approximately 3 mW without EOM modulation. The pump power is saturated for modes of smaller $|l|$. The black squares represent the storage efficiencies achieved by independently optimizing the pump power for different $|l|$. A slower decay in storage efficiency can be observed because of the Gaussian spatial profile of the pump beam. For a pump light with super-Gaussian spatial profile, a homogeneous and optimized storage efficiency should be achievable for all modes.

Some of the SLM patterns for the generation and detection of the superposition states $|\psi_\pm(l)\rangle$ are depicted in Fig. S13. Clearly, a higher resolution of the SLM is required for the generation of modes with higher $|l|$. The spatial intensity profiles of some of the generated modes at the sample position are depicted in the Fig. S14. The measurements are performed by reflecting the beams to a CCD camera placed at a position corresponding to the sample but outside the cryostat.

The intensity of the beam center for OAM states of $|\psi_\pm(l)\rangle$ should always be zero. However, for $|l| > 10$, a bright center can be observed for the generated beam because the small diameter of the beam at the SLM and the limited spatial resolution of the SLM. This phenomenon is expected to be responsible for the decrease in visibility of the input states with higher $|l|$, as shown by the black squares in Fig. 3c in the main text.

There is a typical problem when the SLM and SMF are utilized to analyze the OAM states. As already noted in Ref. [12], the conversion between OAM modes and Gaussian modes cannot be realized completely accurately. This is because that although the phase can be flattened, the field retains its ringed intensity pattern and is therefore a nontrivial superposition of radial modes. Due to the fact that only fundamental radial modes can be coupled into SMF, the coupling efficiency decreases for converted OAM modes. In our experimen-

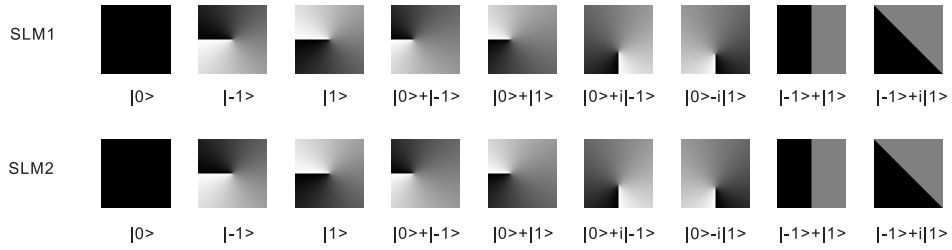

Fig. S11: SLM patterns for quantum state tomography of entanglement. The normalization coefficients are omitted for simplicity.

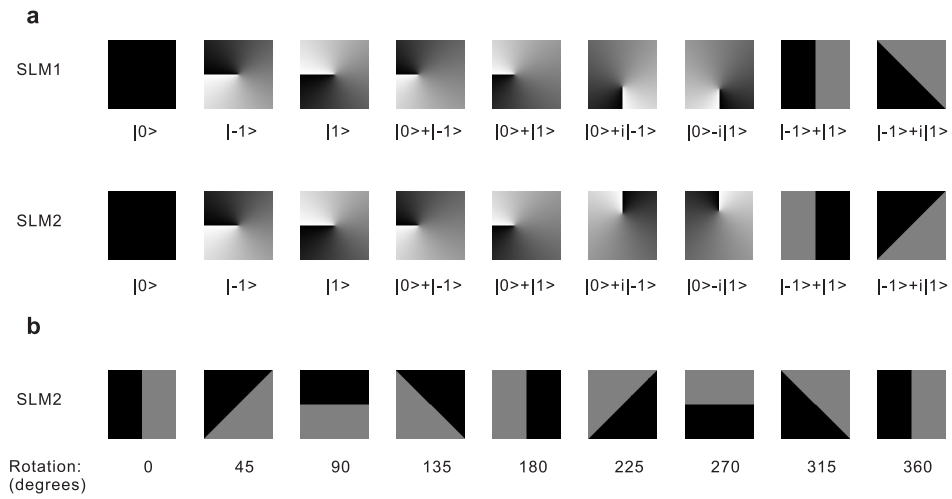

Fig. S12: SLM patterns for quantum process tomography (a) and measurements of the storage performance for the input state $|-1\rangle + |1\rangle$ (b).

t, the SMF coupling efficiency for converted states with $|l| = 25$ decreases to approximately 28%. Because the SMF post-selects the photons, this problem only affects on the coupling efficiency but does not decrease the visibility of superposition states. This low collection efficiency suggests that the SLM and the SMF is no longer a good analyzer for very-high-dimensional OAM states. The use of an OAM mode sorter [13, 14] and direct detection with a photon detector are likely to be better solutions in future studies.

Final remarks

Rare-earth (RE)-doped solids have been shown to possess a considerable capability for storing photons with extended life time [15], high fidelity (see Ref. [16] and also this work), large bandwidth (see Ref. [17] and also this work), high efficiency [18] and multimode capacity in the temporal domain [19], the spectral domain [20] and the spatial domain (this work). Recently, remarkable progress has been achieved, including the spin-wave storage of single-photon-level pulses [21] and an unprecedentedly long spin coherence time achieved in Eu:YSO crystal [22]. The further exploitation of these remarkable properties should enable the RE-doped solids to find fascinating applications in both quantum and classical information processing.

[1] L. Allen, M. W. Beijersbergen, R. J. C. Spreeuw and J. P. Woerdman, *Phys. Rev. A* **45**, 8185 (1992).
[2] A. Vaziri, J. W. Pan, T. Jennewein, G. Weihs,and A. Zeilinger, *Phys. Rev. Lett.* **91,** 227902 (2003).
[3] A. C. Dada, J. Leach, G. S. Guller, M. J. Padgett and E. Andersson, *Nature Phys.* **7,** 677 (2011).
[4] R. Inoue, T. Yonehara, Y. Miyamoto, M. Koashi and M. Kozuma, *Phys. Rev. Lett.* **103,** 110503 (2009).

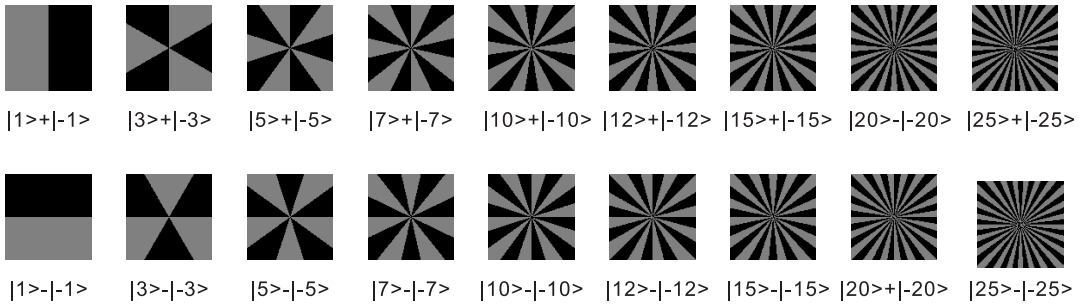

Fig. S13: SLM patterns for the generation and detection of the superposition states $|\psi_{\pm}(l)\rangle$.

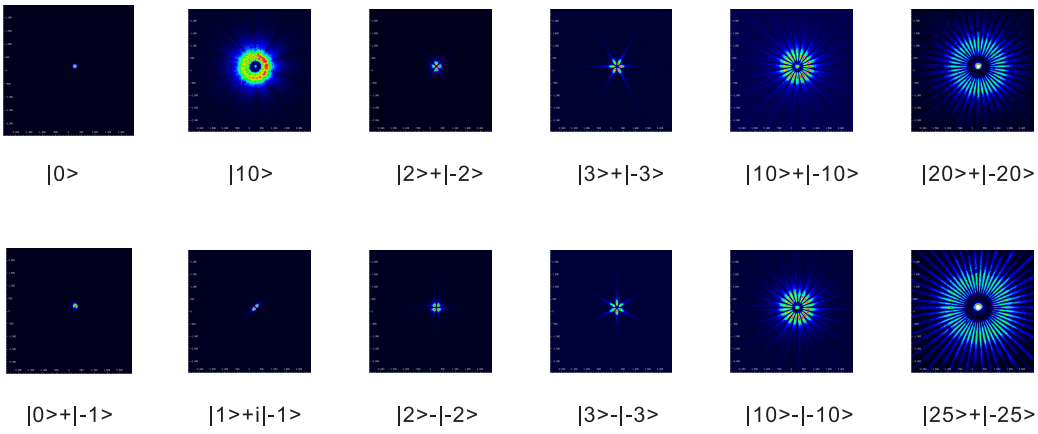

Fig. S14: Measured intensity profiles of various states at the sample position.

[5] M. J. Padgett, *et al.,* New J. Phys. 17, 023011 (2015).
[6] M. Afzelius, C. Simon, H. de Riedmatten and N. Gisin, *Phys. Rev. A.* **7**9, 052329 (2009).
[7] F. Bussières, *et al. Nature Photonics* **8**, 775 (2014).
[8] D. Collins, N. Gisin, N. Linden, S. Massar and S. Popescu, *Phys. Rev. Lett.* **8**8, 040404 (2002).
[9] Z. Q. Zhou, S. F. Huelga, C. F. Li and G. C. Guo, arXiv:1209.2176v2 (2014)
[10] J. L. O'Brien, *et al. Phys. Rev. Lett.* **93,** 080502 (2004).
[11] R. T. Thew, K. Nemoto, A. G. White and W. J. Munro, *Phys. Rev. A* **66,** 012303 (2002).
[12] H. Qassim, *et al. J. Opt. Soc. Am. B* **3**1, A20 (2014).
[13] M. Mirhosseini, M. Malik, Z. Shi and R. W. Boyd, *Nature Commun.* **4**, 2781 (2013).
[14] G. C. G. Berkhout, *et al. Phys. Rev. Lett.* **1**05, 153601 (2010).
[15] G. Heinze, C. Hubrich and T. Halfmann, *Phys. Rev. Lett.* **1**11, 033601 (2013).
[16] Z. Q. Zhou, W. B. Lin, M. Yang, C. F. Li and G. C. Guo, *Phys. Rev. Lett.* **1**08, 190505 (2012).
[17] E. Saglamyurek, *et al. Nature* **4**69, 512 -515 (2011).
[18] M. P. Hedges, J. J. Longdell, Y. Li and M. J. Sellars, *Nature* **4**65, 1052 (2010).
[19] M. Bonarota, J.-L. Le Gouèt and T. Chanelière, *New Journal of Physics* **1**3, 013013 (2011)
[20] N. Sinclair, *et al. Phys. Rev. Lett.* **1**13, 053603 (2014).
[21] P Jobez, *et al. Phys. Rev. Lett.* **1**14, 230502 (2015).
[22] M. Zhong *et al. Nature* **5**17, 177 (2015).